The Influence of Sea Surface Temperature on the Tropical Intraseasonal Oscillation: A Numerical Study

TIANMING LI* AND BIN WANG

Department of Meteorology, University of Hawaii, Honolulu, Hawaii

(Manuscript received 1 October 1993, in final form 2 March 1994)

ABSTRACT

The development and movement of the tropical intraseasonal system (TIS) exhibit remarkable annual variations. It was hypothesized that spatial and temporal variation in sea surface temperature (SST) is one of the primary climatic factors that are responsible for the annual variation of TISs. This paper examines possible influences of SST on the TIS through numerical experiments with a 2.5-layer atmospheric model on an equatorial β plane, in which SST affects atmospheric heating via control of the horizontal distribution of moist static energy and the degree of convective instability.

The gradient of the antisymmetric (with respect to the equator) component of SST causes a southward propagation of the model TIS toward northern Australia in boreal winter and a northward propagation over the Indian and western Pacific Oceans in boreal summer. The phase speed of the meridional propagation increases with the magnitude of antisymmetric SST gradients. The poleward propagation of the equatorial disturbance takes the form of moist antisymmetric Rossby modes and influences the summer monsoon.

During May when SST is most symmetric in the western Pacific, a disturbance approaching the date line may evolve into westward-moving, double cyclonelike, symmetric Rossby modes due to the suppression of the moist Kelvin mode by the cold ocean surface east of the date line. The disturbance over the equatorial Indian Ocean, however, may evolve into an eastward-moving, moist Kelvin–Rossby wave packet; meanwhile, a cyclonic circulation may be induced over the Gulf of Thailand and Malaysia, drifting slowly westward into the Indian subcontinent.

1. Introduction

The activity of the Madden–Julian oscillation (MJO) is season dependent. Madden (1986) showed that the zonal wind anomaly in the 40–50-day timescale exceeds that in adjacent lower- and higher-frequency bands by the largest amount during December–February. Similar conclusions were reached by Gutzler and Madden (1989). Hendon and Salby's (1994) study indicates that strong annual and interannual variations in the strength of the oscillation exist.

The observed Madden–Julian oscillation exhibits also considerable spatial variability. Knutson and Weickmann (1987) first produced a life cycle of the oscillation based on a 6-yr composite EOF (empirical orthogonal function) analysis. They found that in the Eastern Hemisphere the upper- and lower-troposphere circulation anomalies couple with convection and move slowly eastward at a speed of about 5 m s^{-1}, whereas in the Western Hemisphere only upper-tropospheric circulation anomalies are evident, which travel at a speed about three times faster after they decouple from convection anomalies. On the basis of a composition of 36 outgoing longwave radiation (OLR) anomaly events, Rui and Wang (1990) suggested a four-stage life cycle: initiation over equatorial Africa; rapid development passing through the equatorial Indian Ocean; mature evolution characterized by an intermittent weakening over the Indonesian archipelago and reintensification over the western Pacific warm pool; and a final decay near the date line or emanation from the equatorial central Pacific toward subtropical North America and the southeastern Pacific.

In addition to prevailing eastward propagation, Yasunari (1979, 1980) found the northward propagation of cloud bands with a typical speed of about 1° latitude per day that is associated with the equatorial MJO. Krishnamurti and Subrahmanyam (1982) documented meridional propagation of a train of troughs and ridges from the equator to about 30°N over the Indian summer monsoon region with a phase speed of about 0.75° latitude per day. Lau and Chan (1986) found that during eastward propagation of the intraseasonal oscillation, there are two branches of meridional propagation of negative OLR (convection) anomalies: northward toward the Indian subcontinent and northwestward to-

* Current affiliation: Program in Atmospheric and Oceanic Sciences, Princeton University, Princeton, New Jersey.

Corresponding author address: Prof. Bin Wang, Department of Meteorology, University of Hawaii at Manoa, 2525 Correa Road HIG 331, Honolulu, HI 96822.

ward the northwestern Pacific/South China Sea. The activity of the MJO is found to have profound influences on the onset, active/break, and retreat of the Indian summer monsoon (e.g., Sikka and Gadgil 1980; Krishnamurti 1985; Hartmann and Michelson 1989) and the Australia monsoon (Holland 1986; Murakami et al. 1986; Hendon and Liebmann 1990). The meridional propagation was also found in general circulation model experiments (e.g., Lau and Lau 1986; Hayashi and Golder 1986).

The MJO detected by cross-spectral analysis of the wind fields reflects statistical behavior of tropical intraseasonal variation. From a dynamical point view, it is more meaningful to identify and examine individual intraseasonal disturbances whose collective behavior produces MJO. Based on this working hypothesis, Wang and Rui (1990a) defined objectively tropical intraseasonal convective anomalies using a pentad-mean anomaly map of OLR. Strong convective anomalies are found to be accompanied by dynamically consistent anomalous circulations (Rui and Wang 1990). We will regard them as anomalous dynamical systems and refer to them as tropical intraseasonal systems (TISs).

The movement revealed from pentad-mean anomaly maps of OLR confirmed the above findings and exhibited a more complex picture. Wang and Rui (1990a) identified 122 TISs during a 10-yr period (1975–85 with 1978 missing). Of those, 64% were dominantly eastward, 22% were northward, and 14% were westward. The meridional propagation takes three major tracks (Fig. 1): (a) equatorial eastward-moving TISs turning at 100°E toward either the northwestern Pacific in boreal summer or the South Pacific convergence zone (SPCZ) in boreal winter; (b) equatorial eastward-moving TISs splitting over the Indian and/or western Pacific Oceans with separate centers moving northward; and (c) independently northward movement over the Indian monsoon and the western North Pacific monsoon regions that is not associated with equatorial eastward-moving systems. The eastward-moving TIS not only occurs more frequently but also has a larger amplitude from November through April, whereas the independent northward-moving TISs occur only from May to October. The westward-moving systems have smaller spatial scales and relatively weak intensities. They are observed primarily about one Rossby radius of deformation (10°–15° of latitude) away from the equator and in the summer hemisphere (Fig. 1c). Cadet (1983), Murakami (1983), and Nakazawa (1988) also found westward-propagating cloud anomalies west of the date line.

The observational discoveries have prompted interest in developing theoretical models to understand and interpret the spatial and temporal variations of TISs. Several key questions related to the observed phenomena are the following: 1) What factors are responsible for the significant spatial variations of the activity of TISs? 2) What causes the considerable seasonality and other temporal variability of the oscillation? 3) What physical processes determine meridional and westward propagation of TISs in a monsoon domain?

Murakami et al. (1984) postulated that the low-frequency modes propagate northward and have maximum amplitude near 10°–20°N through mutual interactions between synoptic-scale disturbance, the local Hadley circulation, and the zonal mean flows over the northern summer monsoon region. Slow northward propagation on a timescale of 20–40 days was simulated in terms of zonally symmetric monsoon models (Webster 1983; Goswami and Shukla 1984; Gadgil and Srinivasan 1990). Webster proposed that the land-surface latent and sensible heat fluxes in the boundary layer, which destabilizes the atmosphere ahead of the ascending zone, were the principal cause of the northward propagation. Lau and Peng (1990), on the other hand, investigated the interaction between a large-scale monsoon circulation and an equatorial Kelvin wave disturbance. As an equatorial Kelvin wave passes the Indian summer monsoon longitude, unstable baroclinic disturbances are generated over India, which causes a rapid northward shift of the rising branch of the local Hadley circulation. They argue that the vertical shear of basic-state monsoon circulation is essentially important for the unstable development.

Given the fact that there are large SST gradients and land–sea thermal contrasts along the north–south direction over the monsoon region, it is conceivable that inhomogeneous SST and moist static energy distribution may contribute to meridional propagation of TIS. The dependence of the development and propagation speed on SST suggests that the annual march of SST could be one of the major climatic factors that is responsible for the observed spatial dependence and annual variation of TIS (Wang and Rui 1990b). The motivation of this present study is based on these conjectures. The objective of this study is to identify and understand the possible influence of underlying SST variations on the intraseasonal oscillation by means of numerical experiments.

To achieve this goal, we shall extend the model of Wang and Li (1994) to include SST effects in a more realistic manner. In section 2, a brief description of the model and the way SST affects the dynamics is given. In section 3 and 4, the development, propagation, and structure of the TIS in a climatological January and July SST background are simulated and investigated. The model suggested an important relationship between meridional propagation of TIS and the north–south SST gradients. In section 5, we examine the behavior of moist Rossby and Kelvin waves in SST distribution in transitional seasons. A summary is given in the last section.

2. The model

The physical and numerical aspects of the model used in this study have been described in Wang and Li

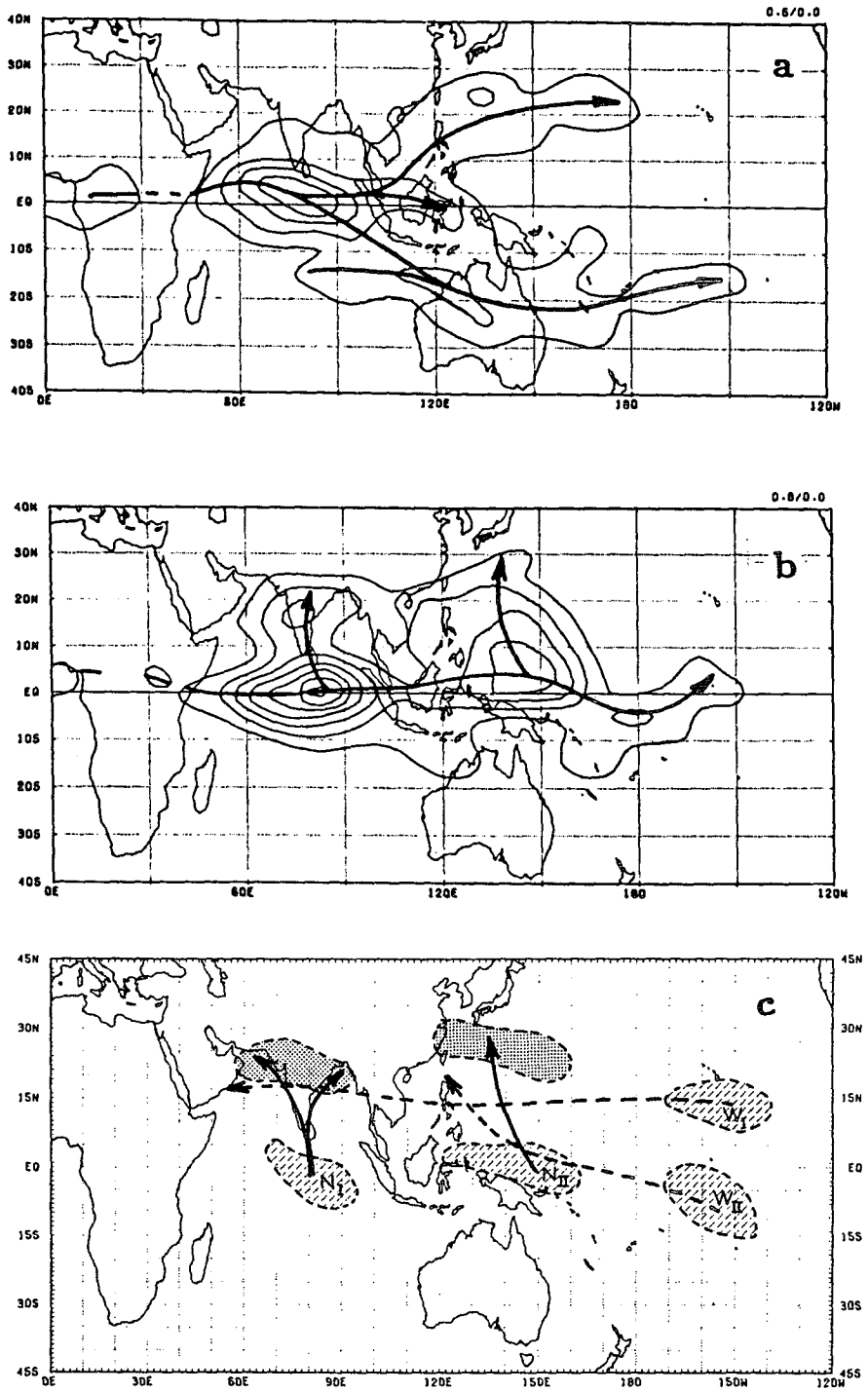

FIG. 1. Schematic diagrams showing the three types of meridional propagation of TISs by thick solid arrows. Panels (a) and (b) show meridional propagations that are associated with equatorial eastward propagations. The thinner contours are frequency of occurrence of the center of eastward-propagating TISs at each 2° × 2° box that contain meridional propagating components. Panel (c) shows tracks of meridional propagations that are independent of equatorial eastward propagation. Shown in (c) are also tracks of westward propagation (adopted from Wang and Rui 1990a).

(1994). For this reason, we will describe only the model physics via which SST affects atmospheric motion without detailed derivation of the equations.

To focus on the convection–frictional convergence feedback mechanism, we do not consider the evaporation–wind feedback process in the present study. The governing equations on an equatorial β plane are

$$\frac{\partial u}{\partial t} - \beta y v = -\frac{\partial \phi}{\partial x} - \epsilon u + r\nabla^2 u, \quad (2.1a)$$

$$\frac{\partial v}{\partial t} + \beta y u = -\frac{\partial \phi}{\partial y} - \epsilon v + r\nabla^2 v, \quad (2.1b)$$

$$\frac{\partial \phi}{\partial t} + C_0^2(1 - \delta I)\nabla\cdot\mathbf{V} = C_0^2 d(\delta B - 1)\nabla\cdot\mathbf{V}_B - \epsilon\phi + r\nabla^2\phi, \quad (2.1c)$$

$$E_1 u_B - \beta y v_B = -\frac{\partial \phi}{\partial x}, \quad (2.1d)$$

$$E_2 v_B + \beta y u_B = -\frac{\partial \phi}{\partial y}, \quad (2.1e)$$

where $\mathbf{V}(u, v)$ and $\mathbf{V}_B(u_B, v_B)$ are the lower-free-troposphere and boundary layer winds, respectively; ϕ stands for the lower-free-troposphere geopotential; ϵ is the Rayleigh friction or Newtonian cooling coefficient in the free atmosphere (10^{-6} s^{-1}); r is the horizontal momentum diffusion coefficient (6×10^5 m^2 s^{-1}); C_0 = 40 m s^{-1} denotes the dry gravity wave speed of the free-troposphere baroclinic mode; $E_1 = E$ and $E_2 = 3E$ are zonal and meridional Rayleigh friction coefficients in the boundary layer and E denotes the Ekman number that depends on turbulent viscosity in the boundary layer, surface and boundary layer depth, and surface roughness length (Wang 1988); $d = (p_s - p_e)/\Delta p$ is the nondimensional depth of the boundary layer.

In the thermodynamic equation (2.1c) the convective heating is parameterized by a simplified Kuo's (1974) scheme; that is, the heating rate is determined by the precipitation rate that is the product of a precipitation efficiency coefficient and the sum of the boundary layer and lower-troposphere moisture convergence. The nondimensional parameter $I = (q_3 - q_1)/S$ is a heating coefficient associated with wave convergence, and $B = q_e/S$ is a heating coefficient associated with frictional convergence. The parameter S stands for an equivalent vertical mean specific humidity in the lower-tropospheric layer that could make effective static stability vanish in the presence of wave-convergence-induced heating (Wang and Li 1994); its value depends on C_0 or dry static stability of the free troposphere and the precipitation efficiency coefficient (0.65). Quantities q_e, q_3, and q_1 are the vertical mean specific humidities in the boundary layer, the lower-tropospheric layer, and the upper-tropospheric layer, respectively. Here q_1 is taken as a constant (0.0004); q_e and q_3 are given by

$$q_e = \frac{q_0(p_s^m - p_e^m)}{m(p_s - p_e)} \quad (2.2a)$$

$$q_3 = \frac{q_0(p_e^m - p_2^m)}{m(p_e - p_2)}, \quad (2.2b)$$

where p_s, p_e, and p_2 are nondimensional pressure at the surface (1000 mb), the top of the boundary layer (900 mb), and the middle of the free troposphere (500 mb), respectively; $m = H/H_1$ with H = 7.6 km being the density scale height; H_1 = 2.2 km the water vapor density scale height; and q_0 the surface air specific humidity that is assumed to be a function of SST, T_s (°C), given by the following empirical regression equation:

$$q_0 = (0.972T_s - 8.92) \times 10^{-3}. \quad (2.3)$$

The empirical relation (2.3) is derived from climatological monthly mean SST and surface air specific humidity averaged at each 2° × 2° latitude–longitude box for the entire tropical Pacific Ocean (30°S–30°N, 120°E–80°W). The data are derived from original Comprehensive Ocean–Atmosphere Data Set (COADS). The sample size is 28 800 and the correlation coefficient is 0.99.

Note that the moisture content (q_e and q_3) is a linear function of SST so that the heating intensity coefficients I and B are directly controlled by SST. They vary with space. Such inhomogeneous distributions of moist static energy are expected to have profound influence on the developing and propagating characteristics of the intraseasonal oscillation.

Since we focus on the influence of gross SST distribution, the surface temperature over the land was interpolated from SST of the adjacent ocean. The specific humidity on land surface was estimated using (2.3). To take into account land effects on humidity, the estimated specific humidity was reduced by 30% over the winter hemisphere land areas for the January and July experiments. Over North Africa, the estimated specific humidity was reduced by 70% for all seasons to mimic the dry conditions of Sahel. These modifications were based on climatological humidity distribution over the land.

The model heating scheme is nonlinear in the sense that the heating rate depends on large-scale motions; that is, condensational latent heating is released only in the region where the precipitation (p_r) is positive. In addition, the switch-on of the convective heating is assumed to depend on SST, following Wang and Li (1993):

$$\delta = \begin{cases} 1, & \text{if } p_r > 0 \text{ and } T_s > 26.5°\text{C} \\ 0.5(T_s - 24.5), & \text{if } p_r > 0 \text{ and } 24.5°\text{C} < T_s < 26.5°\text{C}, \\ 0, & \text{otherwise} \end{cases} \quad (2.4)$$

where p_r represents total moisture convergence in the vertical air column. The dependence of convective

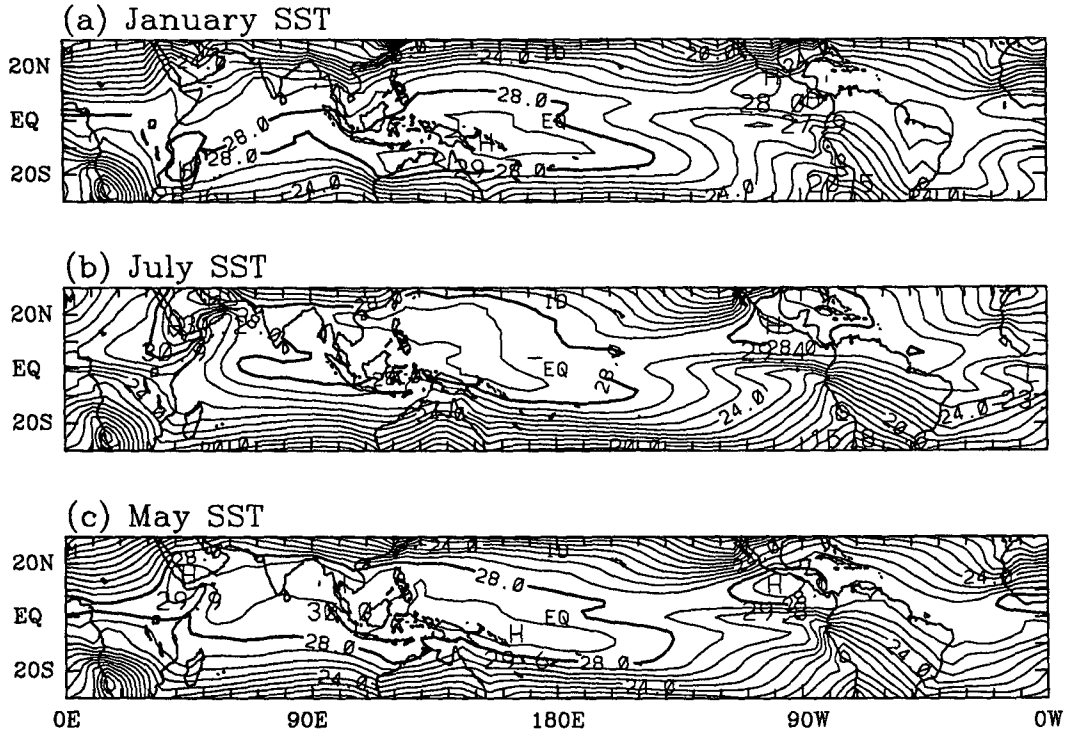

FIG. 2. Climatological (a) January, (b) July, and (c) May mean sea surface temperature in the Tropics. Temperature over the land is interpolated (fictitious). Data are derived from Sadler et al. (1987). The contour interval is 1°C. The thicker solid line represents 28°C.

heating on SST is based on the observed tendency for the tropical atmosphere to be more convectively unstable over warm ocean. In a statistical sense, the time-averaged degree of conditional instability may be depicted as a function of SST. Waliser and Graham (1993) showed how deep convection, as inferred from outgoing longwave radiation or highly reflective clouds, varies with SST over the tropical ocean. The dependence of the heating switch-on function on SST simulates qualitatively the influence of SST on deep tropical convection, based on their observed relationship.

The structure of an initial intraseasonal disturbance is specified as an equatorial Kelvin wave, Rossby wave, or a coupled Rossby–Kelvin wave forced by an anomalous atmospheric heating, following Gill's (1980) solutions. Climatological monthly mean SST fields derived from the COADS for 80 years (1900–79) by Sadler et al. (1987) are used in the present study.

3. Northern winter experiment

Observational studies have indicated that there is a close association between the Australian monsoon activity and the tropical intraseasonal oscillation (Murakami et al. 1986; Holland 1986; Hendon and Liebmann 1990; Zhu and Wang 1993). In this section, we attempt to examine how an equatorial intraseasonal disturbance develops and propagates as it passes through the Indian and Pacific Oceans. Climatological January mean SST is used as a northern winter condition.

The initial perturbation is a solitary Kelvin wave located at 40°E at the equator. We integrated the model for a time period of 30 days.

a. Longitudinal dependence of development and zonal propagation

The climatological January mean SST field (Fig. 2a) exhibits a large variation along the equator. The highest SST (29.7°C) occurs in the western Pacific warm pool, whereas the lowest SST (less than 25°C) appears in the eastern Pacific. A second highest SST (28.5°C) is located in the eastern Indian Ocean (80°–100°E).

Figure 3 shows that the zonal-mean precipitation rate for the TIS is about 3 mm day^{-1}, and the maximum precipitation rate in the western Pacific is 9 mm day^{-1}. The maximum precipitation along the equator occurs at day 14 when the TIS is just over the warmest ocean surface (160°E). Another precipitation peak occurs at day 5 when the TIS moves in the eastern Indian Ocean (90°E). A moderate decay is found over the maritime continent (100°–120°E) because the background land-surface temperature is somewhat lower than the surrounding ocean. Rapid decay in the precipitation rate and boundary layer zonal wind takes place in the cen-

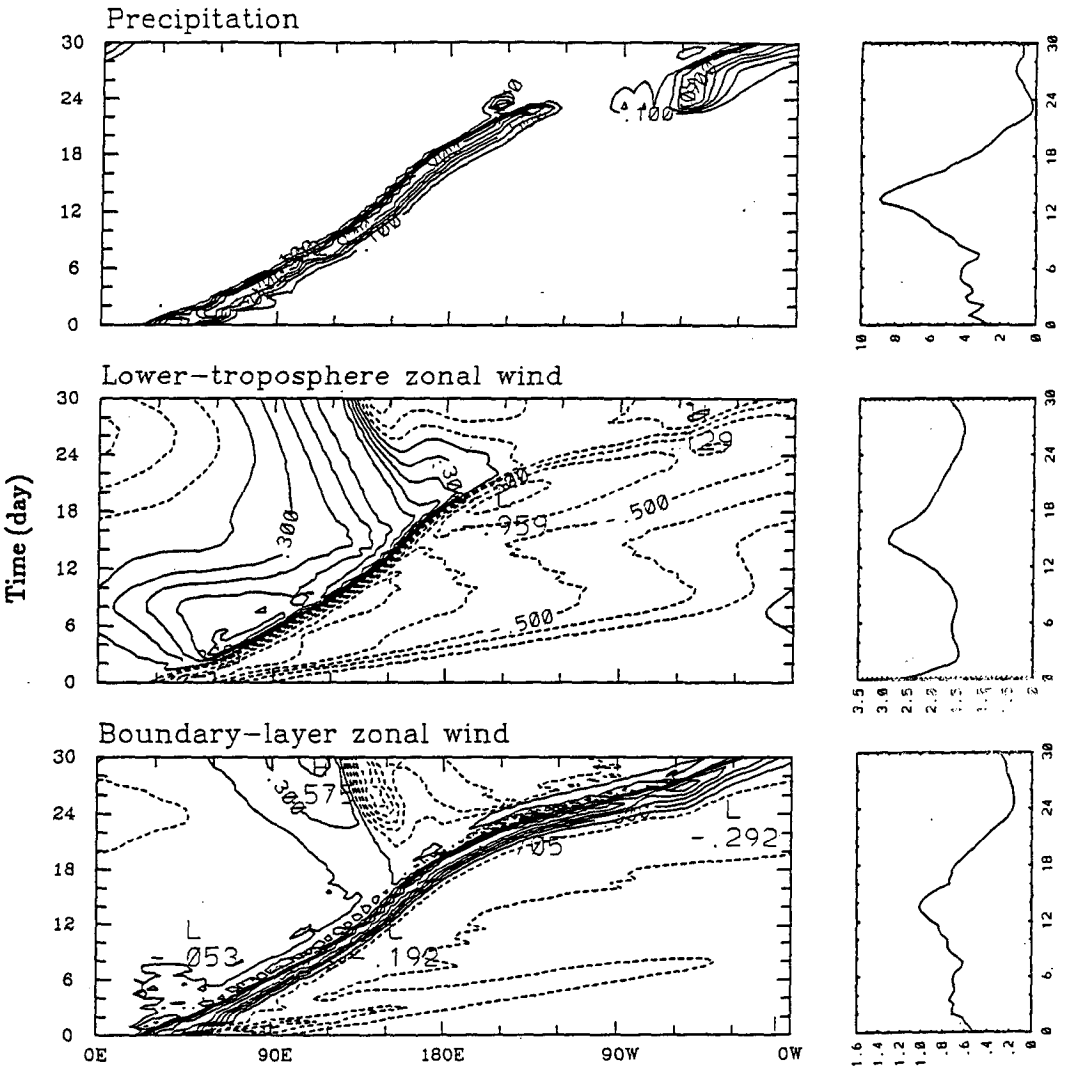

FIG. 3. Time–longitude plots of precipitation, lower-free-tropospheric zonal wind, and boundary layer zonal wind along the equator simulated using climatological January mean SST. The precipitation (mm day^{-1}) and wind (m s^{-1}) fields have been normalized in terms of their maximum values at each time step. The maximum values are shown in rhs panels as a function of time (days).

tral Pacific east of the date line because SST there decreases rapidly eastward. After the disturbance travels across South America (day 24), convection starts to redevelop over the Atlantic intertropical convergence zone (ITCZ). Such a life cycle appears to be in qualitatively good agreement with that of a composite OLR anomaly studied by Rui and Wang (1990) for the northern winter season.

Similar to the rapid decay of convection, the boundary layer wind associated with the disturbance is also confined to the equatorial Indian and western Pacific Oceans: its amplitude drops dramatically east of the date line. The upper- (or lower) free-tropospheric wind anomalies, however, show a clear signal to traverse the Western Hemisphere. The amplitude of the free-tropospheric wind over the eastern Pacific Ocean experiences only a moderate decrease. The amplitude of zonal wind in the free troposphere is 3 m s^{-1}, whereas it is merely 1 m s^{-1} in the boundary layer. In comparison, the observed 850-mb zonal wind speed is twice as large as the boundary layer zonal wind speed (Harrison and Gutzler 1986).

It is interesting to note that the TIS propagates eastward along the equator with a longitude-dependent phase speed. The slowest movement occurs in the western Pacific (approximately 5° longitude per day), whereas the fastest propagation is observed in the eastern Pacific (about 20° longitude per day). This is comparable to the observation of Knutson and Weickmann (1987). In the present model, SST affects the internal

gravity wave speed through changing moist static stability by SST-dependent heating. Therefore, it is expected that the TIS propagates slower during its intensification over the Indian and western Pacific Oceans and much faster in the eastern Pacific where SST is much lower and convection ceases.

b. Enhancement of the Australian monsoon

Figure 4 shows the time evolution of precipitation and lower-tropospheric wind fields. As the convective complex associated with the disturbance propagates eastward along the equator, it deviates southward over the summer monsoon region north of Australia. The reason for this is that the SST maximum is located south of the equator at the Gulf of Capenteria (Fig. 2a). The north–south SST gradients tend to deform and shift the precipitation area toward warmer ocean surface, causing the meridional propagation of perturbation energy, and stimulating convective instability over the warm ocean. This is evidenced by the continuing occurrence of precipitation cells in the Australia monsoon region even after the equatorial disturbance has moved away from the region. The maximum vorticity centers are evidently biased toward the Southern Hemisphere (figure omitted).

As the disturbance travels eastward to the western and central Pacific, Rossby waves are excited from the convection region with a major branch shifting southward to the east of New Guinea, the warmest pool in the world. After the major leading cell reaches the eastern Pacific (at day 24), equatorial convection weakens

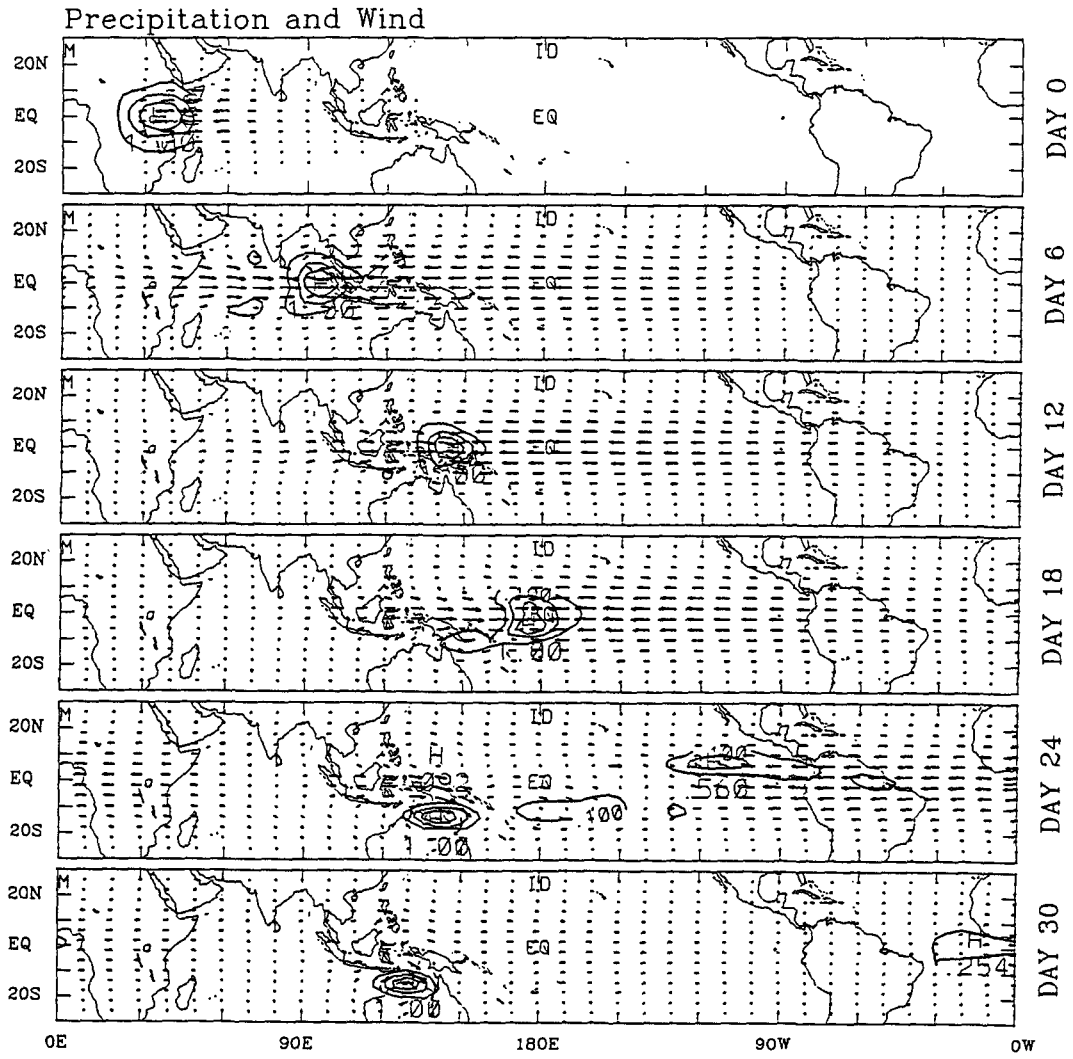

FIG. 4. Time evolution of the horizontal structure of precipitation and lower-tropospheric wind, simulated using January mean SST at day 0, 6, 12, 18, 24, and 30. The precipitation and wind fields have been normalized in terms of their maximum at each time step. Maximum precipitation rates and wind speeds at day 0, 6, 12, 18, 24, and 30 are 2.5, 4.2, 6.9, 5.3, 4.3, and 14.4 mm day^{-1}, and 2.8, 1.6, 2.1, 2.3, 2.3, and 6.2 m s^{-1}, respectively.

dramatically and the convection shifts to the Northern Hemisphere along the SST maximum zone, enhancing ITCZ. The results indicate that the inhomogeneous SST distribution causes the meridional shift of the equatorial convective system and further leads to enhanced wave activity in the monsoon and ITCZ region.

The horizontal structure of the lower-tropospheric wind is dynamically consistent with the precipitation field. For an initial Kelvin wave, the low pressure center is in phase with the maximum easterly. Due to convection–frictional convergence feedback induced heating, equatorial westerlies are generated and develop to the west of the maximum precipitation region (day 6 of Fig. 4). The westerlies accompany an eastward-propagating heat source. As the equatorial westerlies pass over the maritime continent and the western Pacific, two large-scale cyclonic vortices are generated over the Australian monsoon and near the date line south of the equator (day 24). The north Australian cyclone interacts with convective heating and leads to further development of the monsoon circulation (day 30). This suggests a possible influence of the TIS on the Australian summer monsoon.

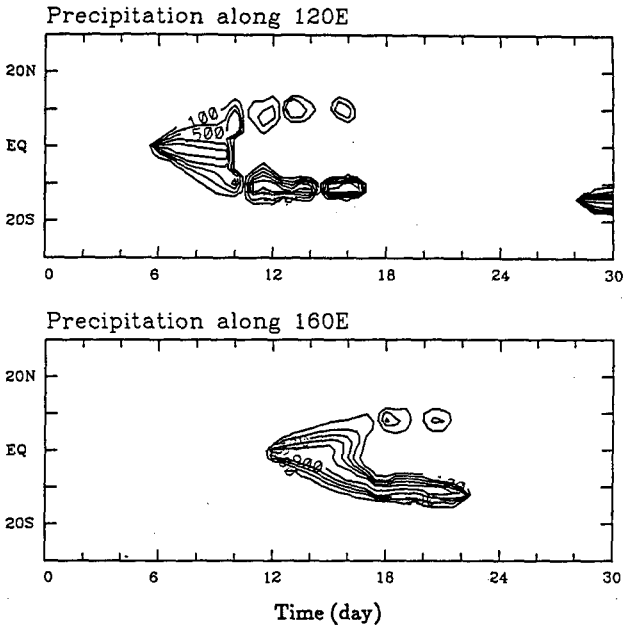

FIG. 5. Time–latitude plot of normalized precipitation along 120°E (upper panel) and 160°E (lower panel) derived from the northern winter experiment. The contour interval is 0.2.

c. *Meridional propagation*

Figure 5 shows the time–latitude section of precipitation along 120° and 160°E. To clearly illustrate meridional phase propagation, the precipitation has been normalized in terms of its maximum values at each time. Therefore, the phase is defined as the contour line of the maximum value of unity.

It should be noted that there is poleward propagation of precipitation cells dominantly southward. As the equatorial disturbance moves to the north of Australia (120°E) at day 6, convection shifts southward toward the Australian summer monsoon region. When the disturbance continues to move eastward to the western Pacific (160°E) at day 12, the convection shifts to the south again toward the warmest ocean surface north of the SPCZ. The mean meridional phase speed is about 1° latitude per day. The southward propagation of convection may play an important role in causing convective instability in the Australian monsoon region.

The SST field can be expressed as a sum of a symmetric (with reference to the equator) and an antisymmetric component (Wang 1994). The symmetric component has a maximum at the equator and decreases poleward, whereas the antisymmetric component vanishes at the equator and increases its magnitude toward midlatitudes. The antisymmetric SST component describes gross thermal contrast between the Southern and Northern Hemisphere and is related to monsoon variations. The meridional propagation is found to be related to the antisymmetric SST distribution, that is, the north–south SST gradients in the antisymmetric SST field. For instance, along 120°E there are two distinct latitude zones in terms of mean antisymmetric SST gradients. The mean gradient between 8° and 14°S (−0.12°C per degree latitude) is three times as large as that between 0° and 6°S (−0.04°C per degree latitude). Correspondingly, the phase speed of the precipitation center between 0° and 6°S is much slower than that between 8° and 14°S. The antisymmetric SST distribution is responsible for the meridional propagation and may be important in determining the phase speed of the meridional propagation.

4. Northern summer experiments

In this section, we demonstrate that perturbations with different horizontal structures and geographical locations may result in a variety of tracks and development patterns, under the influence of the climatological July mean SST (Fig. 2b).

Consider first an initial equatorial intraseasonal disturbance with a Kelvin wave structure located at 40°E. The time series of the horizontal structure of precipitation and lower-tropospheric wind fields are illustrated in Fig. 6. The change of intensity and phase speed with longitude is determined by the longitudinal variation of SST in a similar manner as that in the winter experiments. When the equatorial convective complex propagates eastward to the Indian monsoon region, convection extends progressively northward toward the Indian subcontinent. At day 6 there is a weak convective cell remaining in the tip of the Indian subcontinent, while the main convective area moves to 100°E. When the disturbance reaches the western Pacific (140°E) at day

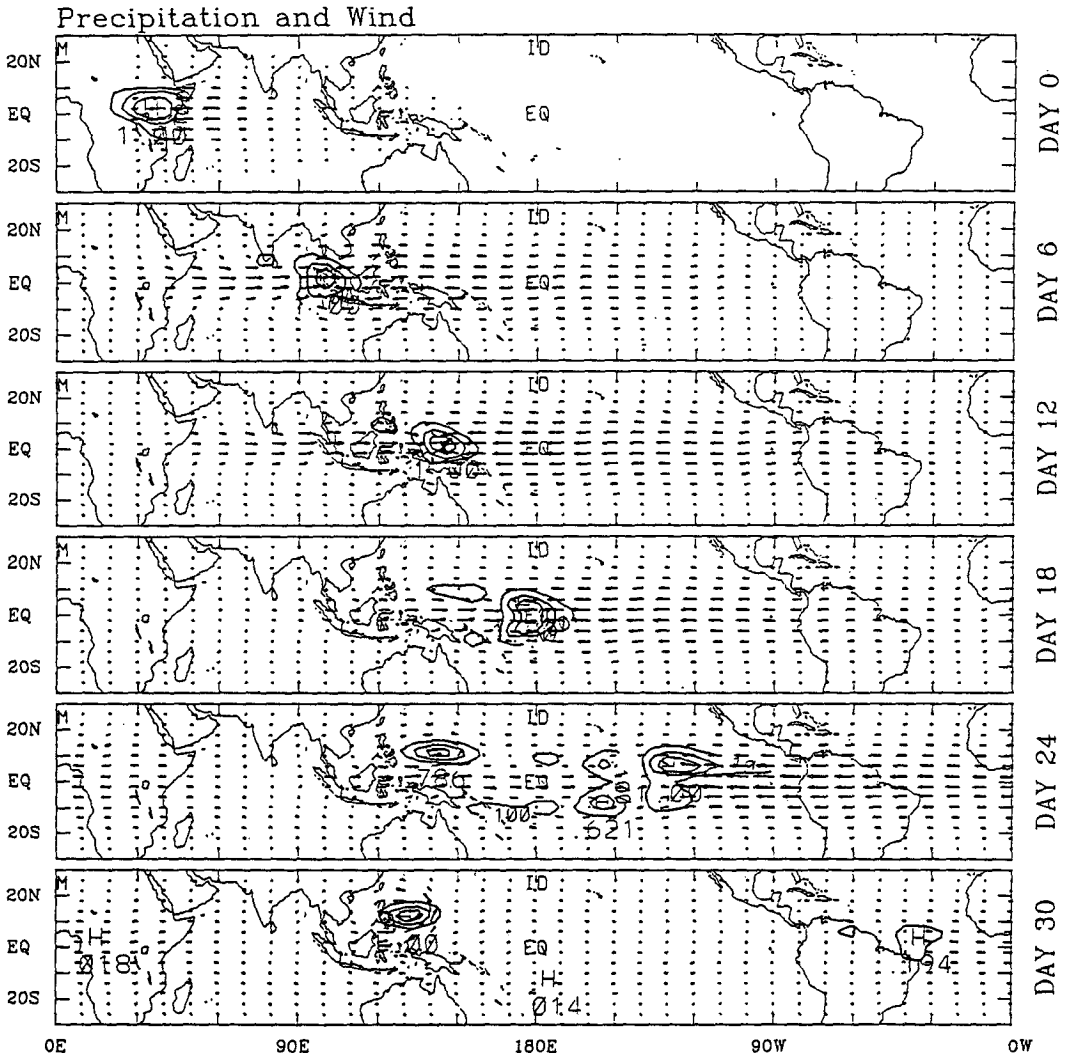

FIG. 6. As in Fig. 4 except for the use of the July mean SST background. The amplitudes of precipitation and lower-tropospheric wind fields at day 0, 6, 12, 18, 24, and 30 are 2.8, 8.2, 10.3, 7.1, 2.7, and 6.1 mm day^{-1}, and 3.2, 2.2, 2.6, 2.9, 1.9, and 2.4 m s^{-1}, respectively.

12, another convective cell develops south of the Philippines. As the disturbance moves to the central and eastern Pacific, convection at the equator is suppressed and maximum precipitation shifts to the north or/and south and tends to develop along the climatological convergence zones. Meanwhile, underlying warm water in the northwestern Pacific Ocean reinforces convection and provides a positive feedback between convective heating and cyclonic circulations. As a result, at day 24, a large-scale cyclonic circulation develops east of the Philippines (10°N, 130°E).

Unstable development of convection and large-scale vortices in the northwestern Pacific, again, is partially due to the meridional propagation of perturbation energy associated with the equatorial disturbance. Figure 7 shows time–latitude profiles of the precipitation field along 80° and 140°E. It is obvious that there is a prominent northward propagation of convection belts originating from the equatorial region. When the equatorial disturbance moves to the central Indian Ocean or east of New Guinea, a branch of convective cells starts to shift to the north although the main body of the equatorial convective complex still moves eastward. The averaged meridional propagation speed is approximately 1° latitude per day.

When an initial perturbation is centered at the equatorial Indian Ocean at 90°E with a structure of a Rossby wave, its subsequent northward drift can be shown by the location of the maximum precipitation centers along 80°E (Fig. 8a). Initially, the maximum convection lies at the equator. Due to the convection–frictional convergence feedback, maximum convection

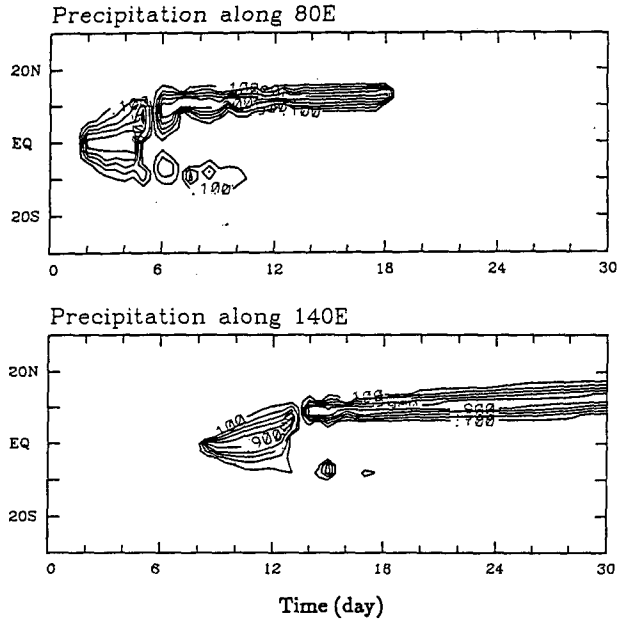

FIG. 7. Time–latitude plot of normalized precipitation along 80°E (upper panel) and 140°E (lower panel) derived from the northern winter experiment. The contour interval is 0.2.

drifts away from the equator and coincides with maximum vorticity centers associated with the equatorial Rossby wave. The selection for most unstable development of convection north of the equator is attributed to the warmer ocean surface in the northern Indian Ocean. The averaged northward propagation speed of maximum convection along 80°E is about 1.2° latitude per day.

Eighteen westward-moving TISs during 1975–85 with a total longitudinal displacement larger than 60° and a duration longer than four pentads are identified (Wang and Rui 1990a). The main path of the westward-propagating mode is confined to the Northern Hemisphere Tropics and subtropics from the central or western Pacific to Southeast Asia or India. Consider an initial intraseasonal disturbance located at 180° on the equator with the structure of a pure Rossby wave. Figure 8b shows the path of maximum precipitation centers associated with the moist equatorial Rossby wave for a time period of 60 days. The maximum convection moves west-northwestward from the equatorial central Pacific (180°) to the Indian subcontinent. The path is qualitatively similar to the observed one, suggesting that the westward-propagating TIS may be a moist equatorial Rossby wave selected by asymmetric meridional SST distribution.

5. Transitional season experiments

January and July SST fields have a significant antisymmetric (w.r.t. the equator) component that causes meridional propagation of the disturbances toward the thermal equator and impacts summer monsoons. In this section, we examine the effect of SST in transitional seasons that is more symmetric w.r.t. the equator than winter or summer.

The meridional variation of the symmetric SST component has a large impact on moist equatorial wave instability. The previous linear stability analysis showed that both the equatorial Kelvin wave and Rossby wave with the lowest meridional structure can be destabilized by interacting with convective heating when SST exceeds a critical value (say 27.5°C) (Wang and Rui 1990b). In the presence of a symmetric SST background (resembling an annual mean SST over the Indian or western Pacific Oceans) in which SST decreases with increasing latitude, the moist static energy in the atmosphere also decreases poleward. As such, the growth of the moist Kelvin wave that has a maximum moisture convergence at the equator is favored. We have performed one experiment with such an idealized symmetric SST field. The initial disturbance was Gill's (1980) steady solution, which consists of an equatorial Kelvin wave and a Rossby wave with the gravest meridional structure. Initially, the convection associated with the moist Kelvin wave moves eastward, whereas the convective system associated with the moist Rossby wave propagates westward. However, the Kelvin wave grows faster and eventually becomes a dominant mode. The result implies the importance of meridional variation of the symmetric component of SST on the equatorial wave selection.

Climatological May mean SST is taken as a representative SST distribution for transitional seasons. It has a maximum warm water belt along 10°N over the Indian Ocean and is nearly symmetric in the western Pacific (Fig. 2c). The asymmetry of the May SST over the Indian Ocean tends to favor the amplification of the

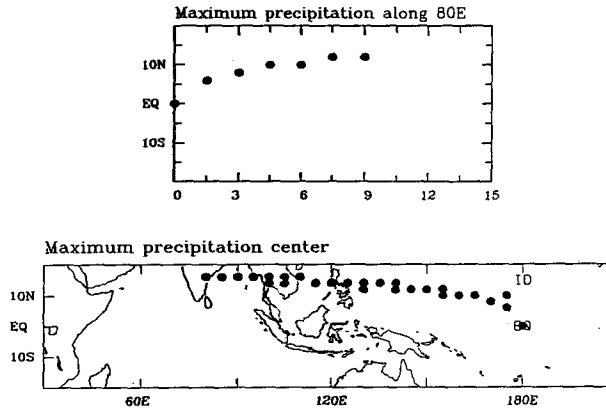

FIG. 8. (a) The northward movement of the maximum precipitation center along 80°E for a disturbance initially located in the equatorial eastern Indian Ocean. (b) The westward propagation of the maximum precipitation center for a disturbance initially located at the equator and the date line. The July mean SST is used in the experiments. The time interval for the precipitation center is 2 days.

moist Rossby wave with an asymmetric meridional structure in the pressure field. Consider an equatorial disturbance with a coupled Rossby–Kelvin wave structure (Gill's solution) centered at 40°E and the equator. Figure 9 shows that when the disturbance passes the equatorial Indian Ocean, the Rossby wave component tends to amplify faster, as evidenced by the maximum precipitation center biased to the north of the equator. This is attributed to high SST (>29°C) around 10°N between 65° and 90°E. The eastward-propagating disturbance is significantly enhanced over the Gulf of Thailand due to the highest SST (30°C) there. Due to the continuous tendency of generation of Rossby waves by the boundary layer convergence, the eastward-propagating disturbance retains its coupled Kelvin–Rossby wave structure. It is interesting to note that as the equatorial convective system passes over the maritime continent, it splits into two systems. At day 18, the equatorial one moves to 150°E; meanwhile, a stronger precipitation cell develops over the Gulf of Thailand. Well-defined cyclonic circulation accompanies and interacts with the precipitation cell. The system continues to intensify and slowly moves westward toward the Indian subcontinent. This experiment suggests that an eastward-moving equatorial MJO may induce development of low pressure systems over the warm water of the Gulf of Thailand in May, which subsequently propagates westward in the form of a moist Rossby wave.

Symmetric SST distribution in the western Pacific in May favors eastward propagation of a coupled Kelvin–Rossby system. It is the sharp decrease of SST east of

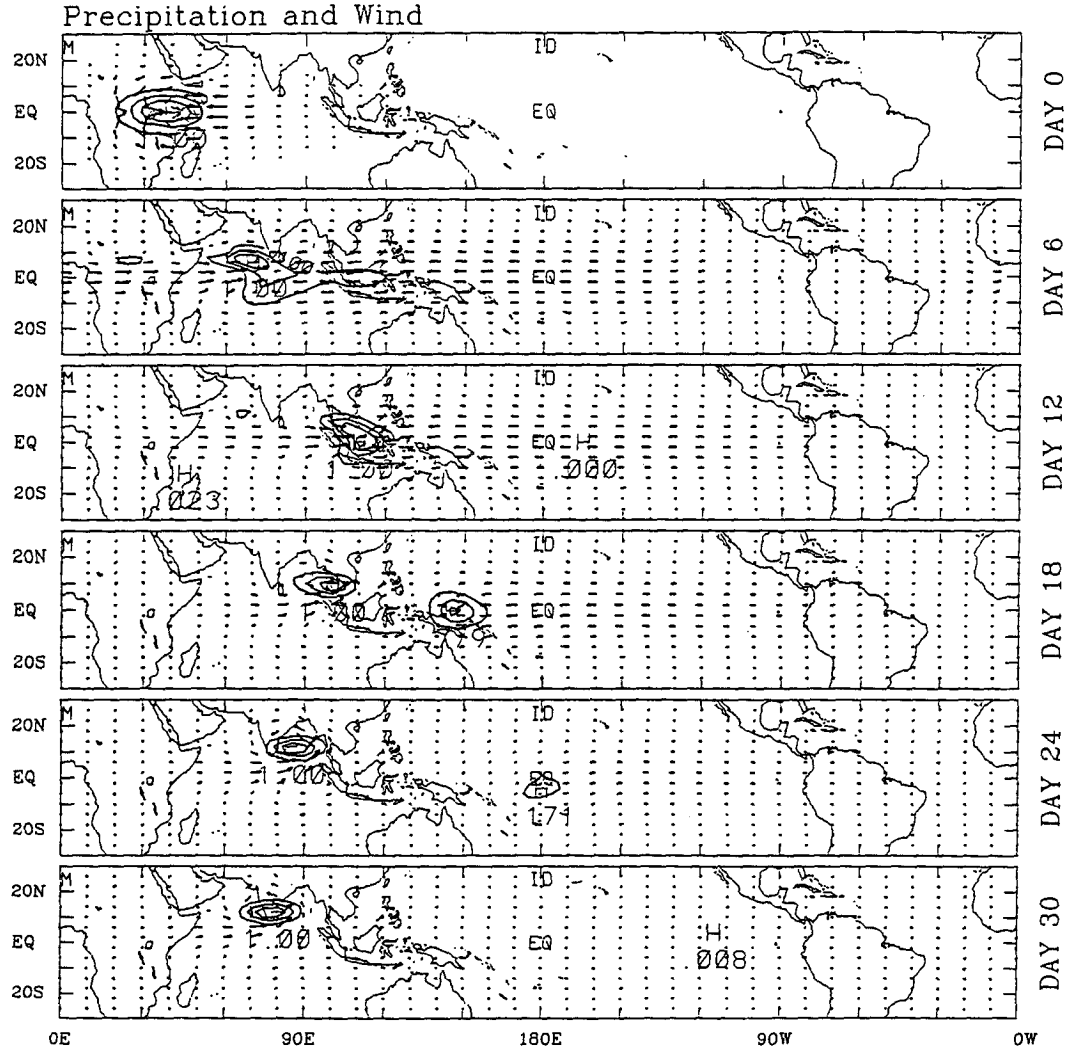

FIG. 9. As in Fig. 4 except for the use of May mean SST background. The initial disturbance is a coupled Rossby–Kelvin wave located at 40°E and the equator. The amplitudes of the precipitation and wind fields at day 0, 6, 12, 18, 24, and 30 are 4.5, 3.2, 5.6, 9.1, 23.9, and 94.5 mm day^{-1}, and 1.6, 1.5, 2.0, 2.8, 8.5, and 35.6 m s^{-1}, respectively.

the date line that prohibits eastward propagation of the Kelvin wave component, yielding a westward emanation of symmetric moist Rossby modes. Figure 10 depicts such a process. Initially, a disturbance with the structure of a coupled Kelvin–Rossby wave is placed at 180° on the equator. The model selects the westward-propagating Rossby wave as the most unstable mode. The eastward-propagating Kelvin wave, on the other hand, rapidly decays because of the low SST in the eastern Pacific. There are two convective centers about 10° latitude away from the equator associated with the unstable Rossby waves. This pattern is reminiscent of double cyclones often occurring in transitional seasons (May and November) (Keen 1982). The lasting westerly wind burst associated with the double cyclones was speculated to be an important source for the oceanic downwelling Kelvin waves that carry a depressed thermocline to the eastern Pacific. The two cyclones are not precisely symmetric about the equator, because of the north–south asymmetry in SST. The stronger cyclone occurs south of the equator east of 150°E because the SST maximum is in the Southern Hemisphere. After the cyclones moved west of 140°E, the southern cyclone weakens, whereas strong development occurs north of the equator because the SST maximum is in the Northern Hemisphere west of 140°E. Therefore, during the transitional season the maximum convection associated with the westward-propagating intraseasonal disturbance may quickly shift from one hemisphere to the other.

6. Summary

The development, propagation, and horizontal structure of the unstable tropical modes have been investigated with a 2.5-layer tropical model in a realistic SST background. The model has shown great sensitivity to the SST of the seasonal and spatial variations of the model low-frequency disturbances. The experimental results can be summarized as following:

- Due to the longitudinal variation of SST, the eastward-propagating disturbances experience an intensification when passing the Indian Ocean, a slight decay over the maritime continent, a redevelopment with achievement of maximum amplitude in the western Pacific, and a rapid decay east of the date line. While strong convective activities associated with the 30–60-day oscillations are well confined to the Indian and western Pacific Oceans, the wind and pressure anomalies in the free troposphere may travel across the Western Hemisphere Tropics, although signals in the boundary layer are insignificant. In addition to the aforementioned development characteristics, the phase speed of the equatorial disturbance is also longitude dependent.
- Due to significant antisymmetric (with respect to the equator) SST distribution, there is a southward propagation of convection accompanying the eastward-propagating equatorial waves during the northern winter. The meridional propagation causes the unstable development of convection and large-scale monsoon cyclones over the Australian monsoon domain. Similarly, during the northern summer, the convection associated with the equatorial waves propagates northward over the Indian Ocean and western Pacific Ocean/South China Sea. Due to the northward propagation, convection and large-scale disturbances develop in the Indian subcontinent and the northwestern Pacific monsoon regions. The antisymmetric SST component causes the meridional propagation primarily via changing the spatial distribution of moist static energy and convective instability. A larger SST gradient may result in a faster meridional propagation speed.
- In May, SST in the Indian Ocean reaches maximum around 10°N with the highest SST occurring in the Gulf of Thailand. When a coupled Kelvin–Rossby wave disturbance moves eastward across the Indian Ocean, it retains the coupled wave structure, but the Rossby wave component is locally enhanced near the southern tip of India. Excitation of Rossby waves also occurs near the Malaysian Peninsula due to the highest SST nearby. In the western Pacific, SST is nearly symmetric about the equator and has a remarkable longitudinal variation. When a disturbance having a coupled Kelvin–Rossby wave structure approaches the date line where SST sharply decreases eastward, the Rossby wave component develops while the Kelvin wave component decays. The development of the unstable moist Rossby mode gives rise to double cyclones residing on each side of the equator propagating westward. Changes in north–south asymmetry of SST may cause a switch of the preferred cyclone development from one hemisphere to the other.

The dependence of the instability and propagation speed on SST suggests that the annual march of SST could be one of the major factors that is responsible for the observed annual variations of TISs as hypothesized by Wang and Rui (1990a). Their linear instability analysis indicated that the growth rate of unstable moist Kelvin waves decreases significantly when the maximum SST shifts from the equator (a boreal winter position) to 7.5°N (a boreal summer position), which explains why the strength of eastward-propagating MJO is stronger in boreal winter than in boreal summer (Madden 1986). The present numerical study takes into account seasonal and spatial variabilities of SST and demonstrated possible roles of these variations on the seasonal and spatial variabilities of the tropical intraseasonal systems. It should be pointed out that the parameterization of convective heating in the model is rudimentary, and the sensitivity of the model low-frequency modes to SST is qualitative. In addition to the influence of SST, the effects of monsoon circulation

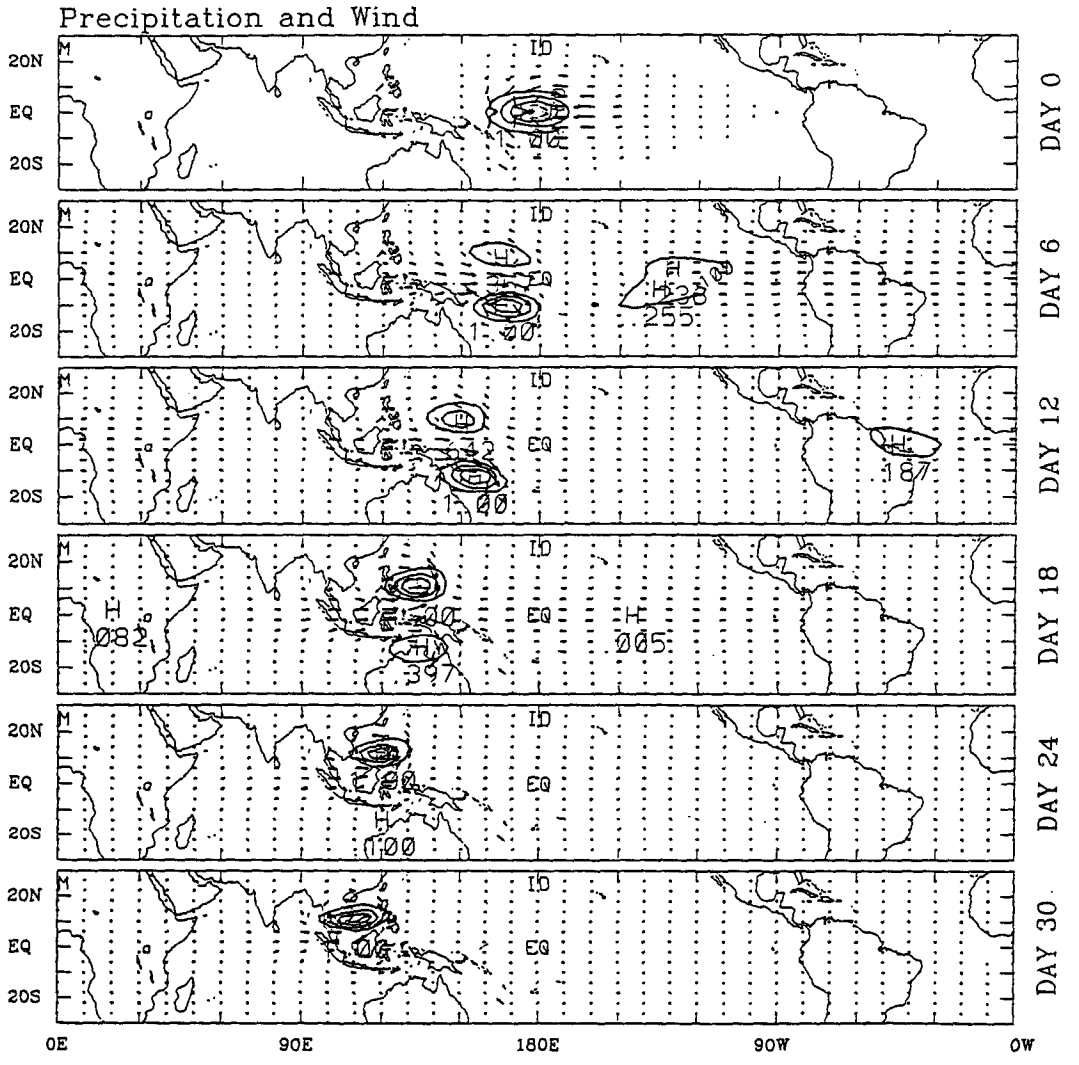

FIG. 10. Same as in Fig. 9 except that the initial disturbance is located at 180°. The amplitudes of the precipitation and wind at day 0, 6, 12, 18, 24, and 30 are 4.2, 3.0, 2.4, 3.4, 14.6, and 51.0 mm day^{-1}, and 1.4, 1.7, 1.6, 1.6, 5.0, and 19.8 m s^{-1}, respectively.

and the Hadley cell may also play fundamental roles in the seasonal variation of TISs. Due to its simplicity, the present model cannot be used to assess the relative importance of SST distribution and mean flow effects. It also neglected SST variations induced by the feedback of the TIS. Further study will focus on examining the effect of climatological mean flows and air–sea interactions on the atmospheric intraseasonal oscillation.

Acknowledgments. Comments by Drs. Gutzler and Sanders as well as an anonymous reviewer led to an improved manuscript. We acknowledge the support made by the Division of Atmospheric Sciences, National Science Foundation under Grant ATM-9019315. This is the School of Ocean and Earth Science and Technology Publication 3588.

REFERENCES

Cadet, D. L., 1983: The monsoon over the Indian Ocean during summer 1975. Part II: Breaks and active monsoons. *Mon. Wea. Rev.*, **111,** 95–108.

Gadgil, S., and J. Srinivasan, 1990: Low frequency variation of tropical convergence zones. *Meteor. Atmos. Phys.*, **44,** 119–132.

Gill, A. E., 1980: Some simple solutions for heat-induced tropical circulation. *Quart. J. Roy. Meteor. Soc.*, **106,** 447–462.

Goswami, B. N., and J. Shukla, 1984: Quasi-periodic oscillations in a symmetric general circulation model. *J. Atmos. Sci.*, **41,** 20–37.

Gutzler, D. S., and R. A. Madden, 1989: Seasonal variations in the spatial structure of intraseasonal tropical wind fluctuations. *J. Atmos. Sci.*, **46,** 641–660.

Harrison, D. E., and D. S. Gutzler, 1986: Variability of monthly averaged surface and 850 mb winds at tropical Pacific islands. *Mon. Wea. Rev.*, **114,** 285–294.

Hartmann, D. L., and M. L. Michelson, 1989: Intraseasonal periodicities in Indian rainfall. *J. Atmos. Sci.*, **46,** 2838–2862.

Hayashi, Y., and D. G. Golder, 1986: Tropical intraseasonal oscillations appearing in a GFDL general circulation model and FGGE data. Part I: Phase propagation. *J. Atmos. Sci.*, **43,** 3058–3067.

Hendon, H. H., and B. Liebmann, 1990: The intraseasonal (30–50 day) oscillation of the Australia Summer monsoon. *J. Atmos. Sci.*, **48,** 2909–2923.

——, and M. L. Salby, 1994: The life cycle of the Madden–Julian oscillation. *J. Atmos. Sci.*, **51,** 2225–2237.

Holland, G. J., 1986: Interannual variability of the Australian summer monsoon at Darwin: 1952–82. *Mon. Wea. Rev.*, **114,** 594–604.

Keen, R. A., 1982: The role of cross-equatorial tropical cyclone pairs in the Southern Oscillation. *Mon. Wea. Rev.*, **110,** 1405–1416.

Knutson, T. R., and K. M. Weickmann, 1987: 30–60 day atmospheric oscillation: Composite life cycles of convection and circulation anomalies. *Mon. Wea. Rev.*, **115,** 1407–1436.

Krishnamurti, T. N., 1985: Summer monsoon experiment—A review. *Mon. Wea. Rev.*, **113,** 1590–1626.

——, and D. Subrahmanyam, 1982: The 30–50 day mode at 850 mb during MONEX. *J. Atmos. Sci.*, **39,** 2088–2095.

Kuo, H.-L., 1974: Further studies of the parameterization of the influence of cumulus convection on large-scale flow. *J. Atmos. Sci.*, **31,** 1231–1240.

Lau, K. M., and P. H. Chan, 1986: Aspects of the 40–50 day oscillation during the northern summer as inferred from outgoing longwave radiation. *Mon. Wea. Rev.*, **114,** 1354–1367.

——, and L. Peng, 1990: Origin of low frequency (intraseasonal) oscillations in the tropical atmosphere. Part III: Monsoon dynamics. *J. Atmos. Sci.*, **47,** 1443–1462.

Lau, N. C., and K. M. Lau, 1986: The structure and propagation of intraseasonal oscillations appearing in a GFDL GCM. *J. Atmos. Sci.*, **43,** 2023–2047.

Madden, R. A., 1986: Seasonal variations of the 40–50 day oscillation in the tropics. *J. Atmos. Sci.*, **43,** 3138–3158.

——, and P. R. Julian, 1971: Detection of a 40–50 day oscillation in the zonal wind in the tropical Pacific. *J. Atmos. Sci.*, **28,** 702–708.

——, and ——, 1972: Description of global-scale circulation cells in the tropics with a 40–50 day period. *J. Atmos. Sci.*, **29,** 1109–1123.

Murakami, M., 1983: Analysis of the deep convective activity over the western Pacific and Southeast Asia. Part II: Seasonal and intraseasonal variations during northern summer. *J. Meteor. Soc. Japan,* **61,** 60–76.

Murakami, T., T. Nakazawa, and J. He, 1984: On the 40–50 day oscillations during the 1979 Northern Hemisphere summer. Part I: Phase propagation. *J. Meteor. Soc. Japan,* **63,** 250–271.

——, L.-X. Chen, and A. Xie, 1986: Relationship among seasonal cycle, low-frequency oscillation, and transient disturbance as revealed from outgoing longwave radiation data. *Mon. Wea. Rev.*, **114,** 1456–1465.

Nakazawa, T., 1988: Tropical super clusters within intraseasonal variations over the western Pacific. *J. Meteor. Soc. Japan,* **66,** 823–839.

Rui, H., and B. Wang, 1990: Development characteristics and dynamic structure of tropical intraseasonal convection anomalies. *J. Atmos. Sci.*, **47,** 357–379.

Sadler, J. G., M. A. Lander, A. M. Hori, and L. K. Oda, 1987: Tropical marine climatic atlas. Vol. 2, Pacific Ocean. Report UHMET 87-02, Department of Meteorology, University of Hawaii, Honolulu, HI, 27 pp.

Sikka, D. R., and S. Gadgil, 1980: On the maximum cloud zone and the ITCZ over Indian longitudes during the southwest monsoon. *Mon. Wea. Rev.*, **108,** 1840–1853.

Waliser, D. E., N. E. Graham, and C. Gautier, 1993: A comparison of the highly reflective cloud and outgoing longwave radiation datasets for use in estimating tropical deep convection. *J. Climate,* **6,** 331–353.

Wang, B., 1988: Dynamics of tropical low-frequency waves: An analysis of the moist Kelvin wave. *J. Atmos. Sci.*, **45,** 2051–2065.

——, 1994: On the annual cycle in the equatorial Pacific cold tongue. *J. Climate,* submitted.

——, and H. Rui, 1990a: Synoptical climatology of transient tropical intraseasonal convection anomalies: 1975–1985. *Meteor. Atmos. Phys.*, **44,** 43–61.

——, and ——, 1990b: Dynamics of the coupled moist Kelvin–Rossby wave on an equatorial beta-plane. *J. Atmos. Sci.*, **47,** 397–413.

——, and T. Li, 1993: A simple tropical atmosphere model of relevance to short-term climate variations. *J. Atmos. Sci.*, **50,** 260–284.

——, and ——, 1994: Convective interaction with boundary-layer dynamics in the development of tropical intraseasonal system. *J. Atmos. Sci.*, **51,** 1386–1400.

Webster, P. J., 1983: Mechanisms of monsoon low-frequency variability: Surface hydrological effects. *J. Atmos. Sci.*, **40,** 2110–2124.

Yasunari, T., 1979: Cloudiness fluctuations associated with the Northern Hemisphere summer monsoon. *J. Meteor. Soc. Japan,* **57,** 227–242.

——, 1980: A quasi-stationary appearance of 30–40 day period in the cloudiness fluctuations during the summer monsoon in India. *J. Meteor. Soc. Japan,* **58,** 225–249.

Zhu, B.-Z., and B. Wang, 1993: The 30–60 day seesaw between the tropical Indian and western Pacific Oceans. *J. Atmos. Sci.*, **50,** 184–199.